Dielectrophoresis Reveals Stimulus-Induced Remodeling of Insulin Granule Subpopulations

Running title: DC-iDEP reveals ISG heterogeneity

*Ashley Archambeau,[1] Teji Korma,[2] Aneesh Deshmukh,[1] Mark A. Hayes,[2] Kate L. White[1,3,4]**

[1]Department of Chemistry, Bridge Institute, USC Michelson Center for Convergent Bioscience, University of Southern California, Los Angeles, CA 90089, USA
[2]School of Molecular Sciences, Arizona State University, Tempe, AZ 85287, USA
[3]Department of Quantitative and Computational Biology, USC Dornsife College of Letters, Arts, and Sciences, University of Southern California, Los Angeles, CA 90089, USA
[4]Lead contact
*Correspondence: katewhit@usc.edu

KEYWORDS

Dielectrophoresis, Separation, Insulin secretory granule, Pancreatic β-cell

ABSTRACT

The pancreatic β-cell contains several functional subpopulations of insulin secretory granules (ISGs). These subpopulations vary in maturity, age, and secretory capacity. Differences in protein and lipid composition of ISGs are correlated with disease but require further study to understand how ISG remodeling regulates normal biology. Due to limitations in traditional separation methods, the extent of these subpopulations, any overlap between them, and how they are affected by insulinotropic signals have not been determined. In this work, we adapted direct current insulator-based dielectrophoresis (DC-iDEP) to separate ISGs isolated from INS-1E cells, an immortalized rat insulinoma cell line model, according to their electrokinetic mobility ratio (EKMr). We were able to separate ISG subpopulations from unstimulated cells to determine a baseline distribution and identify characteristic profiles for immature, young, and old ISGs. We then analyzed distributions of subpopulations from cells stimulated with insulin secretion signals known to induce biophysical remodeling and maturation. We found significant changes in each subpopulation studied in response to stimulation, consistent with the increases in maturation, crystallization, and changes in size reported in the literature. This work provides new insights into how the cell controls ISG remodeling and may improve future development of more effective therapies.

SIGNIFICANCE

Understanding insulin secretory granule (ISG) heterogeneity and the functional role of subpopulations is a critical aspect for unraveling the mechanisms of insulin secretion. We adapted direct current insulator-based dielectrophoresis (DC-iDEP) to resolve immature, young, and old ISG subpopulations based on their biophysical properties. We also explored the biophysical remodeling of ISGs under insulinotropic stimuli to further probe how the cell controls remodeling and secretion. Our work provides a new framework for quantifying granule heterogeneity by linking biophysical features to functional subtypes and assessing how environmental stimuli remodel ISGs. This methodology establishes a broadly applicable platform to interrogate organelle and vesicle diversity in complex biological systems.

INTRODUCTION

Insulin is a peptide hormone essential for blood glucose regulation (1). It is produced by the pancreatic β-cell and packaged into organelles called insulin secretory granules (ISGs), which then undergo a process called maturation in which they are prepared for secretion upon β-cell stimulation (2). ISG maturation involves the acidification of the ISG lumen, conversion of proinsulin to insulin, and insulin condensation or crystallization (3,4). Due to the nature of this process, several ISG subpopulations with varying ages, cargo, secretory capacities, and levels of maturity are present in the β-cell, but the extent of the heterogeneity of ISGs in the β-cell is unclear (5-7). Disease states of the β-cell, such as diabetes, are associated with defects in maturation and changes in ISG subpopulation ratios (6,8). As rates of diabetes rise worldwide, understanding insulin maturation and ISG heterogeneity is crucial (9).

Several functional ISG subpopulations have been identified, such as a readily releasable, docked, and reserve pool, which are primarily defined by their proximity to the plasma membrane (10-13). Other identified subpopulations are defined by the speed of their release and their response to calcium, their age, their pH, or their degree of maturation, among others (5,6,14-16). Of these subpopulations, immature, young, and old ISGs have been found

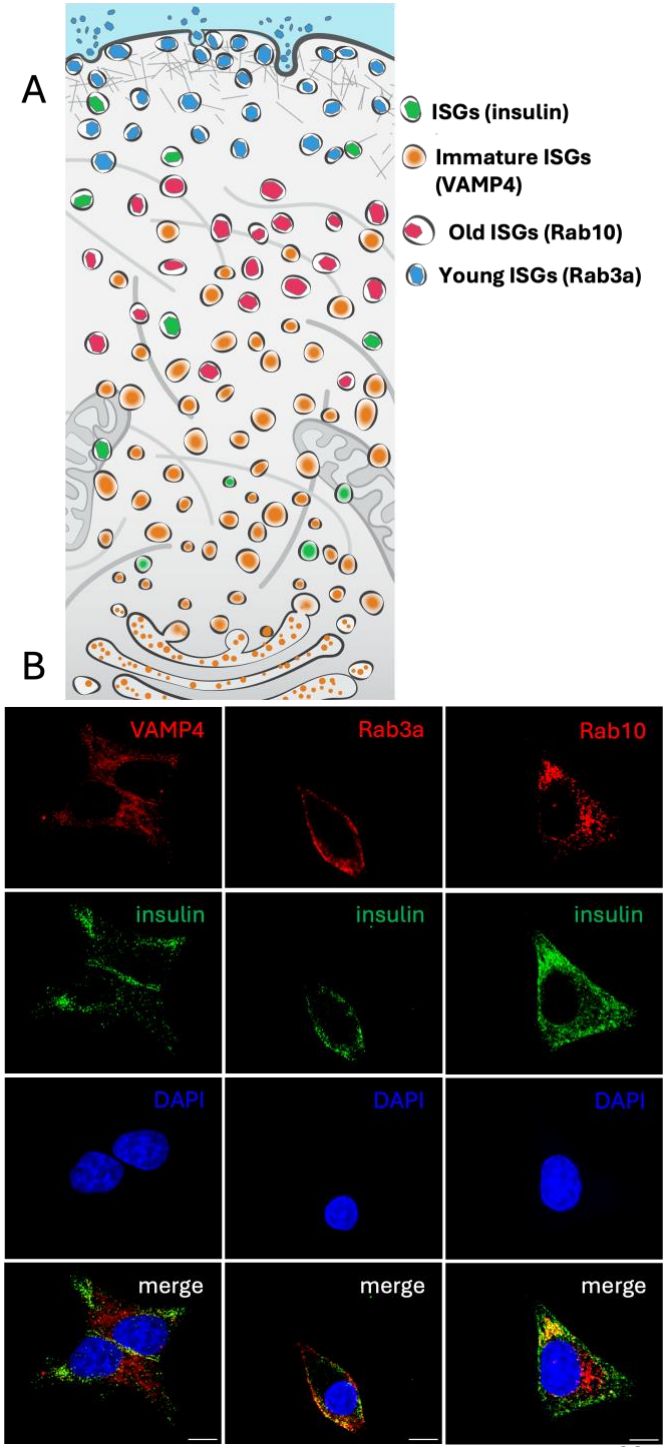

Figure 1. Approach for separating immature, young, and old ISG subpopulations. **A.** These subpopulations undergo remodeling in response to insulinotropic drugs such as TAK-875 and exendin-4 (Ex-4). **B.** Colocalization of ISG subpopulation markers VAMP4, Rab3a, and Rab10 with insulin in INS-1E cells. Scale bar: 5 μm.

to contain VAMP4, Rab3a, and Rab10, respectively (5,7,17) (**Figure 1A**). Rab3a, Rab10, and VAMP4-positive ISGs will henceforth be referred to as young, old, and immature ISGs, respectively, and insulin-positive ISGs will be referred to as ISGs. Immature ISGs are precursors to mature ISGs and are not typically secreted. Young, mature ISGs are more mobile, more acidic, and are preferentially released over older ISGs, while older ISGs are "caged" and targeted for degradation (5,16,18-22). However, gaining a complete picture of the composition of biologically distinct subpopulations has been challenging.

Identification of subpopulations has traditionally required *a priori* knowledge of protein markers to distinguish subtypes using fluorescence microscopy. Alternative approaches of isolating ISGs for follow-up lipidomics and proteomic analysis provide highly heterogeneous results, likely due to differences in specific cellular conditions (7). It has been difficult to isolate ISGs for extensive biophysical characterization, as isolated ISGs often contain contamination by proteins from many other cellular compartments, such as the endoplasmic reticulum, trans-Golgi network, cytoskeletal, lysosomal, and mitochondrial proteins (7,23-30). To better understand the scope of ISG heterogeneity in the β-cell, an unbiased separation method is necessary. Dielectrophoresis has been used in the separation of both biological and nonbiological samples, such as proteins, stem cells, bacterial strains, and gold nanoparticles, among others (31-34). Thus, in our previous work, we established direct current insulator-based dielectrophoresis (DC-iDEP) as an avenue for unbiased separation of ISG subpopulations (35).

DC-iDEP separates particles using a nonuniform electric field based on their electrokinetic mobility ratio (EKMr). Biophysical differences between ISG subpopulations, particularly differences in radius, zeta potential, and conductivity, affect the EKMr values of each subpopulation according to the equation below:

$$EKMr = \frac{\mu_{EK}}{\mu_{DEP}} = \frac{\zeta_p - \zeta_m}{r^2\left(\frac{\sigma_p - \sigma_m}{\sigma_p + 2\sigma_m}\right)\nabla E^2} \quad \textbf{(1)}$$

where μ_{EK} and μ_{DEP} refer to the electrokinetic and dielectrophoretic mobilities, ξ_p refers to the zeta potential of the particle, ξ_m refers to the zeta potential of the medium, r refers to the radius of the particle, σ_p refers to the conductivity of the particle, σ_m refers to the conductivity of the medium, and E refers to the electric field (36). A sawtooth-patterned microfluidic chip is used to accumulate particles with specific EKMr values between the triangular tips, called "gates," that have been designed to have a particular EKMr value (**Figure S1**) (31-34). Barekatain and Liu, et al. used DC-iDEP to separate ISG subpopulations and reported significant changes in the ratios of ISG subpopulations between unstimulated and glucose-stimulated cells (35).

To build on this concept, we include known markers of immature, young, and old ISGs to identify separations of these subpopulations. We also incorporate additional insulinotropic stimuli known to remodel ISGs, such as G-protein-coupled receptor 40 (GPR40) agonists and incretins. GPR40, a free fatty acid receptor, is involved in lipid signaling and the regulation of insulin secretion. Incretins are hormones that increase glucose-stimulated insulin secretion, ISG maturation, and include GLP-1 (glucagon-like peptide-1) and its analogs, and GIP (glucose-dependent insulinotropic polypeptide) (37,38). These two classes of drugs likely enhance ISG maturation differently, producing unique subpopulations (38,39). GPR40 agonists have been found to promote ISG maturation and to increase ISG diameter as the ISG approaches the periphery of the cell (38). The incretin exendin-4 has been found to promote ISG acidification and increase ISG density throughout the cell (16,38).

In this work, we measure the distribution and overlap of ISG subpopulations associated with differences in maturity and age in the INS-1E cell line. We compare the differences in this distribution as a result of orthogonal stimuli: a GPR40 agonist (TAK-875) and an incretin (exendin-4; Ex-4). We show that there are significant differences in the distributions of immature, young, and old ISGs, and that these distributions change in characteristic ways as a result of incretin stimulation and GPR40 agonism. Understanding how unique protein signaling pathways impact ISG maturation and generation of subpopulations is a critical step for unraveling the fundamental mechanisms of secretory biology and future development of effective therapeutics

EXPERIMENTAL METHODS

Cell culture

INS-1E cells (a gift from Pierre Maechler's laboratory at the University of Geneva) were cultured in 5% CO_2 at 37°C. Cells were seeded in optimized RPMI 1640 media (AddexBio C0004-02, supplemented with 5% fetal bovine serum (FBS), 50 μM 2-mercaptoethanol, 1x Penicillin-Streptomycin, and 100 μg/mL streptomycin), sterile filtered through a 0.22 μm filter, and grown to 80% confluency. For each biological replicate, cells were seeded at a density of 4×10^4 cells/cm^2 in one-layer cell chambers (Avantor 734-1038). For stimulation, cells were starved in KRBH buffer containing 0 mM glucose for 30 minutes before stimulation in KRBH containing 25 mM glucose and either 10 nM exendin-4 or 10 μM TAK-875 for 30 minutes.

Colocalization of subpopulation markers with insulin

Cells were grown on ibidi 8-well high ibiTreat slides (80806-96). Cells were fixed with 4% PFA for 10 minutes at 4°C, then stained with a primary antibody cocktail containing guinea pig anti-insulin (1:200, BioSynth 70R-10659) and an ISG subpopulation marker (mouse anti-Rab3a, 1:100 [Synaptic Systems 107 111]; mouse anti-insulin, 1:200 [Cell Signaling Technology 8138S]; rabbit anti-Rab10, 1:100 [Cell Signaling Technology 8127S]; rabbit anti-VAMP4, 1:100 [Synaptic Systems 136 002]) in 0.5% bovine serum albumin (BSA), 0.2% saponin, and 1% FBS in tris-buffered saline (TBS) at 4°C overnight. Excess antibody was removed by three washes with TBST (0.1% Tween-supplemented tris-buffered saline) for 10 minutes, then cells were stained with a secondary antibody cocktail containing Alexa Fluor® 488 AffiniPure™ Goat Anti-Guinea Pig IgG (H+L) (Jackson ImmunoResearch 106-545-003) and either Alexa Fluor® 568 AffiniPure™ Donkey Anti-Mouse IgG (H+L) (Jackson ImmunoResearch 715-575-150) or Alexa Fluor® 568 AffiniPure™ Goat Anti-Rabbit IgG (H+L) (Jackson ImmunoResearch 111-575-144) for 30 minutes at room temperature. Excess antibody was removed by 3 washes for 10 minutes, then cells were mounted in ProLong Glass Antifade Mountant with NucBlue Stain (Thermo Fisher Scientific P36981) and cured for 24 hours before imaging.

Confocal imaging was performed using a Leica Mica microhub equipped with a 63×/1.2NA water immersion objective. The signal was collected with 359, 499, and 650 nm excitations and 461, 520, 668 nm emissions for nuclei, insulin, and ISG subpopulation markers, respectively, by HyD FS detector. The images were deconvoluted by LAS X, lightning module.15-20 planes were collected with a Z-step of 0.16 μm, and a maximum projection of the planes was produced.

Insulin secretory granule enrichment

Cells were harvested with 0.125% trypsin and gently washed in phosphate-buffered saline before being suspended in homogenization buffer (HB, 250 mM sucrose, 150 mM NaCl, 4 mM HEPES, pH 7.4, 1 mM EGTA) supplemented with house-made protease inhibitor (PI) cocktail (0.5 M AEBSF, 1 mM E-64, 1.13 mM leupeptin, and 151.36 μM aprotinin). Following trypsinization, all steps were performed at 4°C. Cells were homogenized by 20 strokes in a Dounce homogenizer, then centrifuged at 1,500×g for 10 minutes to collect cell debris. Supernatant was collected, while the pellet was resuspended in HB supplemented with PI cocktail and subjected to homogenization and centrifugation as described above. The supernatants from both spins were then centrifuged at 5,900×g for 15 minutes to remove larger organelles. The supernatants from that spin were then pooled and centrifuged at 35,000×g for 60 minutes to sediment ISGs. The pellet was then resuspended in 400 μL HB and layered onto a density gradient column formed by two layers of Optiprep supplemented with 1 μM EDTA (Sigma-Aldrich D1556, 3.8 mL of 35% and 0.5 mL of 14.5%) in an open-top thin-wall polypropylene tube (Beckman 326819).

The density column was centrifuged in an SW55i Beckman rotor at 190,000×g overnight to fractionate vesicle populations. The column-containing tube was punctured at the bottom, and 0.4 mL fractions were collected. Enzyme-linked Immunosorbent Assay (ELISA) was used to identify ISG-containing fractions. Similar dilutions were used for each fraction, and the manufacturer's manual was followed for ELISA (Mercodia 10-1250-01). ISG-containing fractions were then pooled, diluted with HB, and centrifuged at 40,000×g for 60 minutes. The pelleted ISGs were resuspended in a low conductivity buffer (LCHB, 0.3 M sucrose, 5 mM MES, pH 6.3), which is compatible with dielectrophoresis studies. Enriched ISG samples were then confirmed to have the expected diameter by nanoparticle tracking analysis.

Western Blotting

To determine the purity of the enriched ISGs, the cell pellet (post-1,500×g-centrifugation), the organelle pellet (post-5900×g-centrifugation), and the final pellet containing enriched ISG samples were mixed with 10× NuPAGE™ Sample Reducing Agent (Invitrogen NP0009) and 2× Novex™ Tris-Glycine SDS Sample Buffer (Invitrogen LC2676). Samples were loaded on Novex™ Tris-Glycine Mini Protein Gels, 10-20% (Invitrogen XP10205BOX) and run in a mini gel tank at 160 V for 60 minutes. Protein on the gel was then transferred to nitrocellulose membranes using min iBlot™ 2 Transfer Stacks (Invitrogen IB23002) in an iBlot 2 dry blotting device (Invitrogen IB21001). The membrane was blocked in 5% BSA in TBST, then incubated with antibodies against marker proteins for ER (SEC61B, Invitrogen PA3-015), endosomes (EEA1, Cell Signaling Technology 2411S), exosomes (CD63, Novus Biologicals NB100-77913), mitochondria (Cytochrome C, Novus Biologicals NB100-56503), lysosomes (LAMP2A, Cell Signaling Technology), and ISGs (synaptotagmin 9, Synaptic Systems 105 053) at room temperature for 5 hrs. Membranes were then washed three times with TBST, then incubated with Alkaline Phosphatase AffiniPure Goat Anti-Mouse IgG (H+L) (Jackson ImmunoResearch 115-055-003) and Alkaline Phosphatase AffiniPure® Alpaca Anti-Rabbit IgG (H+L) (Jackson ImmunoResearch 611-055-215) at room temperature for 1 hr. Membranes were then washed three times with PBST, and bands were visualized with 1-Step™ NBT/BCIP Substrate Solution (Thermo Fisher Scientific 34042).

Visualization of ISGs by cryo-electron microscopy

All animal studies were conducted using procedures approved and conducted per Institutional Animal Care and Use Committee (IACUC) guidelines at the University of Southern California (Animal Use Protocol #21120). Islets from LSL-Salsa6f mice (RRID: IMSR_JAX:031968) and human islets (RRID:SCR _014387, received from the Integrated Islet Distribution Program) were isolated and dissociated into single cells (40). Islet cells or INS-1E cells were deposited onto 200 mesh gold lacey carbon grids (Ted Pella 01894G) and allowed to adhere for 24 hrs in media. For stimulation conditions, cells were starved in KRBH buffer containing 0 mM glucose for 30 minutes before stimulation in KRBH containing 25 mM glucose and either 10 nM exendin-4 or 10 μM TAK-875 for 30 minutes. ISGs were isolated from INS-1E cells as described above. Excess buffer was removed from grids for 2 or 5 s for isolated ISGs or cells, respectively, at 37°C and 97% humidity, then grids were plunge frozen in liquid ethane using a Vitrobot Mark IV (Thermo Fisher Scientific). Grids were clipped using NanoSoft Autogrid rings and clips (MiTeGen M-CEM-NS-11011001).

Autogrids were screened under cryogenic conditions using a 200 kV Glacios Cryo TEM equipped with a Falcon 4 detector (Thermo Fisher Scientific, magnification 13,500× or 93,000×). Mouse and INS-1E cells were additionally imaged as part of tilt series on a 300 kV Krios G3i equipped with a Gatan K3 direct detection camera (Thermo Fisher Scientific, 26,000× magnification), but only frames at 0° tilt were analyzed in this work.

Immunolabeling of ISGs

Isolated ISGs were incubated with 1:100 each of either anti-insulin (Cell Signaling Technology #8138) and anti-VAMP4 (Synaptic Systems 136 002) or anti-Rab3a (Synaptic Systems 107 111) and anti-Rab10 (Cell Signaling #8127) overnight. ISGs were washed with LCHB, then fluorescently labeled by incubation with 1:100 each of an Alexa 488-conjugated secondary antibody (Jackson ImmunoResearch 115-545-146) and an Alexa 568-conjugated secondary antibody (Jackson ImmunoResearch 111-575-144) for two hours. Fluorescently labeled ISGs were then washed once with LCHB to remove excess antibody and finally resuspended in LCHB.

Device fabrication

The microfluidic device was fabricated and designed as described in previous publications (35,41). There are 27 gates (paired triangle tips) ranging in size from 25-73 μm, with wider gates closer to the inlet. The width of the gates decreases approximately 5 μm after every three repeats. Direct current was applied to the inlet and outlet, with potentials of 900 V, 1200 V, and 1500 V tested.

Separation of ISG subpopulations by DC-iDEP

The separation channel was pretreated with 4% BSA for 15 minutes before washing with LCHB. 10-15 μL of an ISG sample was added to the inlet, and the volume in the channel was maintained at the outlet by the addition of LCHB to prevent pressure-driven flow. Direct current was applied at 900 V, 1200 V, and 1500 V using a 3000D

High Voltage Sequencer (LabSmith HVS448), and particles were allowed to move through the channel according to their EKMr values (**Figure 2C**).

Separation experiments were imaged on a Leica DM IL LED Fluo Inverted Laboratory Microscope equipped with an S80/0.30 condenser and a 5×, NA 0.12 objective. Videos were recorded using a Leica Flexacam C1 camera at 1080p resolution and a frame rate of 30 frames per second. A Leica EL6000 external light source was used with a 3-position fluorescence slider for fluorescence excitation.

Normalization

Intensity values were measured for the duration of each recording in three locations per gate: the gate, the PDMS near the gate, and an empty location in the channel using Fiji (42). Each list of intensity values was averaged during a capture event (particles present in gate). Gates containing no capture events were given intensity values of 0. The gate intensity when empty was subtracted from the intensity during a capture event, then normalized to the PDMS and channel.

$$Normalized\ Intensity = \frac{gate_{capture} - gate_{empty}}{\frac{channel + PDMS}{2}} \quad \textbf{(2)}$$

Gates with replicate EKMr values were averaged and finally normalized to the highest intensity in that dataset to account for differences in concentration and fluorophore intensity. These final normalized values were plotted against their respective EKMr values (**Figure S2**).

RESULTS

Localization of ISG subpopulations in INS-1E cells

Immature, young, and old ISG subpopulations were chosen because of known membrane markers of ISG subpopulations that reflect key stages of maturation. Upon fluorescently labeling ISG subpopulation markers for immature, young, and old ISGs, these subpopulations were found to localize to distinct regions of the cell with the expected localization of their respective subpopulation (**Figure 1B**), as found in prior studies (5,16,21,43,44). VAMP4 (immature ISGs) did not significantly colocalize with insulin due to proinsulin not being processed to insulin yet and was primarily found far from the plasma membrane. Rab3a (young ISGs) was present largely at the periphery of the cell and had high colocalization with insulin, suggesting these ISGs are mature and ready for secretion (10,13,45). Rab10 (old ISGs) was mostly present in the interior of the cell, consistent with findings of old ISGs being caged in the interior of the cell (22,46).

Analysis of ISGs post-isolation

Isolated fractions from density gradient centrifugation were analyzed by insulin ELISA. Fractions 8-10 were identified as ISG-containing fractions (**Figure 2D**) and were pooled and analyzed by Western blotting, nanoparticle tracking analysis, fluorescence microscopy, and cryo-electron microscopy (CryoEM). Western blotting showed that ISG (synaptotagmin 9), lysosomal (LAMP2A), and exosomal (CD63) markers were enriched in pooled ISG samples. The presence of the exosomal marker CD63 in isolated ISGs is consistent with the finding of exosomes inside dense core vesicles but may also indicate the presence of contaminants (47). LAMP2A has also been shown to colocalize with ISGs, but its presence may be indicative of potential contamination (29). ER, endosome, and mitochondrial markers were found in cell and organelle lysates but not enriched ISG samples (**Figure 2E**). NTA and CryoEM both confirmed the enriched ISG samples contained particles of the expected size (diameter: 200-500 nm, **Figure 2F-G**) (10,48).

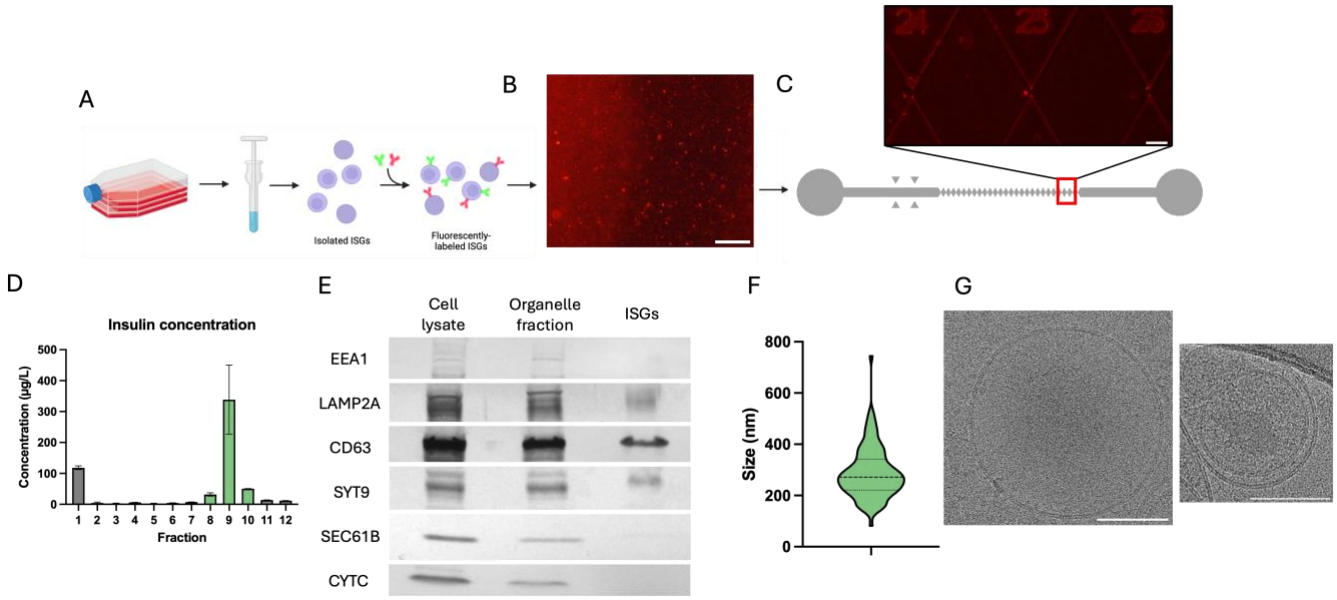

Figure 2. Validation of ISG isolation. **A.** Workflow for isolating ISGs from INS-1E cells. Created in BioRender. **B.** Fluorescence image of isolated ISGs. **C.** Diagram of separation experiments. **D.** Selection of fractions for use in separation experiments. Values are mean ± SEM. **E.** WB of cell lysate, organelle fraction, and isolated ISGs for determination of ISG purity. **F.** Size distribution of ISGs isolated from INS-1E cells. **G.** CryoEM images of isolated ISGs. Scale bars: **B-C**: 250 µm; **G**: 100 nm.

Comparison of ISG subpopulation distributions in unstimulated cells

Separation of ISG subpopulations by DC-iDEP revealed different EKMr distributions of ISG subpopulations (**Figure 3A**). Although three applied voltages were tested (**Figure S3**), 1500 V was selected for further analysis, as this voltage allowed for visualization of ISGs with a wider range of EKMr values (**Figure S4**). This enables a broader separation of subpopulations. Insulin was used as an overall ISG marker, and the superposition of each marker largely correlates with that of insulin (**Figure S5**). The immature ISG marker VAMP4 exhibited a heterogeneous distribution, characterized by a relatively high ratio of low-EKMr ISGs (7). Rab3a, a young ISG marker, had a bimodal EKMr distribution at mid-range values, while the old ISG marker Rab10 displayed a higher ratio of ISGs at high EKMr values (5). To better understand trends in EKMr distribution, the difference in intensities between each pair of EKMr values was calculated and plotted in heat maps for each marker to display the relationship between each subpopulation (**Figure 4B**). Differences between subpopulation markers were analyzed via two-way ANOVA with Bonferroni post hoc correction. Significant differences were found between young ISGs and insulin (2.23×10^{10} V/m^2, p=0.0191), young and old ISGs (9.30×10^{9} V/m^2, p=0.0495; 1.45×10^{10} V/m^2, p=0.0461; 2.23×10^{10} V/m^2, p=0.0178), immature ISGs and insulin (4.10×10^{9} V/m^2, p=0.0251; 1.71×10^{10} V/m^2, p=0.0316), and immature and old ISGs (1.45×10^{10} V/m^2, p=0.0170) (**Figure 3B**). This indicates that each population has distinct distribution patterns due to the biophysical differences in ISGs.

Effect of insulinotropic drugs on ISG subpopulations

To better understand how insulinotropic signals impact ISG remodeling or the generation of distinct subpopulations, we compared stimulated and unstimulated conditions. Both Ex-4 and TAK-875 had significant

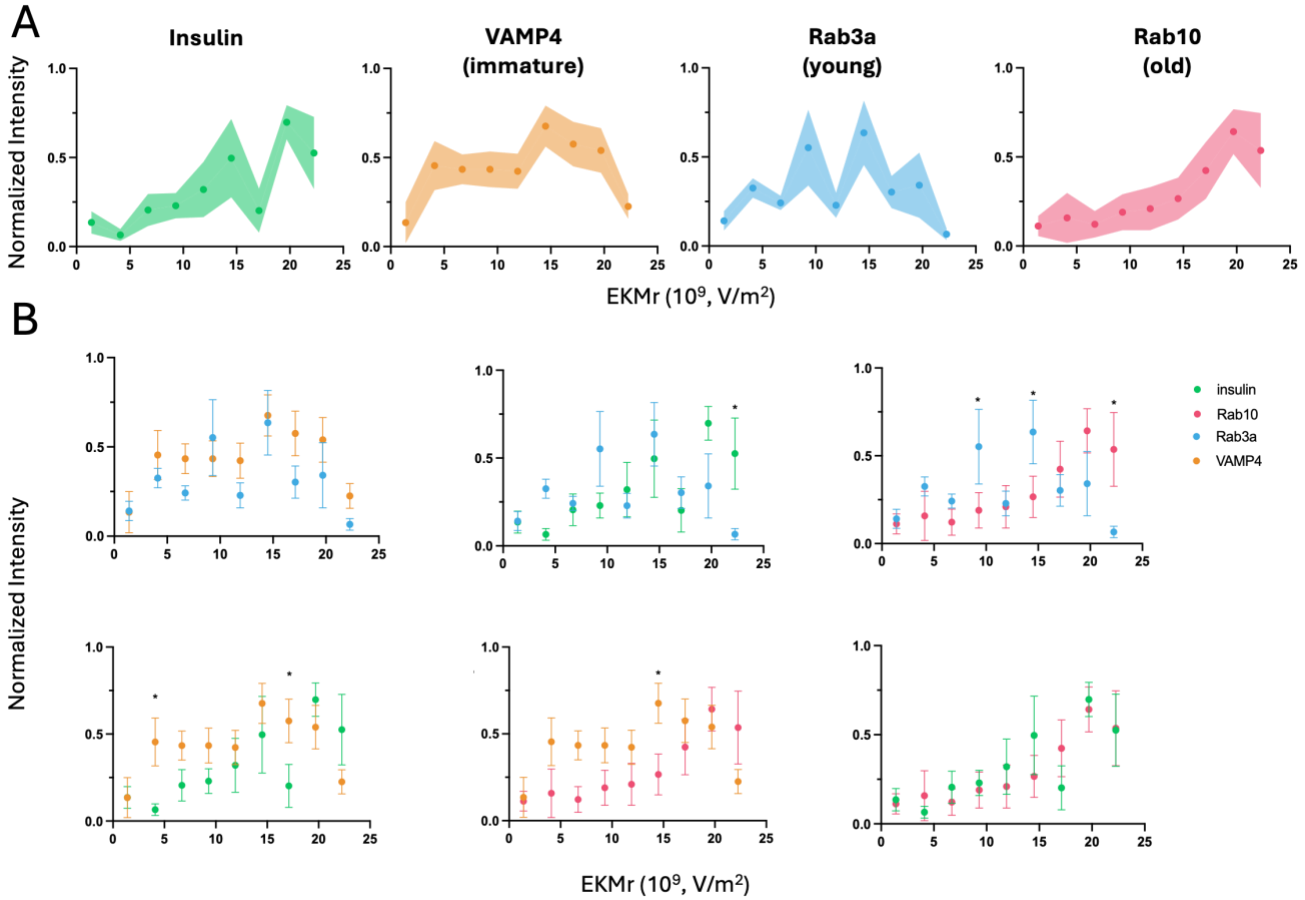

Figure 3. Analysis of ISG subpopulations isolated from unstimulated cells. **A.** EKMr distributions of ISGs in unstimulated cells (n=5-7 for 3-4 biologically independent experiments). **B.** Comparisons of the distributions of different ISG subpopulations. Values are mean ± SEM (*p≤0.05 using ANOVA with Bonferroni post hoc multiple comparison correction).

effects on the EKMr distribution of isolated ISGs when analyzed via two-way ANOVA with Bonferroni post hoc correction, but TAK-875 had a stronger effect on these distributions at all applied voltages (**Figure S6**). TAK-875 had significant effects on the distribution of immature (4.10×10^{9} V/m^2, p=0.0264; 6.70×10^{9} V/m^2, p=0.0345; 1.45×10^{10} V/m^2, p=0.0243), young (1.45×10^{10} V/m^2, p=0.00960), and old (1.19×10^{10} V/m^2, p=0.0417) ISGs (**Figure 4A**). Ex-4 only had a significant effect on young ISGs (1.19×10^{10} V/m^2, p=0.0441) (**Figure 4A**).

The overall distribution of insulin was not largely affected by either TAK-875 or Ex-4, but the shapes of the distribution of immature, young, and old ISGs were altered. When stimulated by either TAK-875 or Ex-4, there was a smaller proportion of ISGs containing VAMP4 at lower EKMr values. Ex-4 led to a peak in the distribution of immature ISGs at 1.45×10^{10} V/m^2, while TAK-875 caused a somewhat bimodal distribution between mid-range and high EKMr values, and a valley at 1.45×10^{10} V/m^2. TAK-875 and Ex-4 both removed the bimodal distribution of young ISGs, with TAK-875 leading to a higher ratio of young ISGs with low EKMr values and Ex-4 producing a more heterogeneous distribution. Both TAK-875 and Ex-4 caused a higher proportion of old ISGs with lower EKMr values than in the unstimulated condition. TAK-875 produced three peaks in the distribution of old ISGs at 4.10×10^{9} V/m^2, 1.19×10^{10} V/m^2, and 1.97×10^{10} V/m^2, and Ex-4 led to a higher ratio of old ISGs at mid-range EKMr values. Additionally, a peak at 1.18×10^{10} V/m^2 appeared in the distribution of both young and old in response to TAK-875.

To further explore the relationships between EKMr values and each condition, we visually display this data using heatmaps made by subtracting the average intensity at one EKMr value from another average value in the same marker and condition (**Figure 4B**). These heatmaps made visualizing similarities and differences between the different markers and conditions easier, as some of the relationships may not be obvious when multiple parameters are overlaid. These heatmaps allowed for the identification of other trends in EKMr distribution in response to

stimulation (**Figure 4B**). For example, in response to Ex-4, a similar peak at 1.45×10^{10} V/m^2 in immature and old ISGs developed (Fig. 4A), which is displayed in the heatmap by a dark horizontal or light vertical band. Similarly, VAMP4 heatmaps show vertical bands at 1.45×10^{10} V/m^2. The unstimulated condition rises slightly, TAK-875 drops, and Ex-4 rises compared with other EKMr values. There were few significant differences between TAK-875 and Ex-4 stimulation, with Ex-4-stimulated cells having a significantly higher ratio of ISGs at 1.45×10^{10} V/m^2 ($p=0.00410$), but the shapes of each were often different (**Figure S7**).

To visualize physical differences in ISGs under these different conditions, we imaged primary mouse β-cells using cryo-electron microscopy. There were observable differences in the appearance of ISGs in unstimulated cells compared with TAK-875 or Ex-4-stimulated cells. Unstimulated cells contained many ISGs with various levels of insulin condensation, as well as some ISGs containing exosome-like structures (47). As expected, based on soft X-ray tomography (SXT) experiments, the number of ISGs present near the cell periphery in TAK-875 and Ex-4 conditions was lower than in unstimulated cells (**Figure 4C**) (38). TAK-875 stimulation caused higher levels of crystallization and more ordered crystals. In this condition, we also observed the presence of dark, unidentified aggregates attached to the cores of some ISGs that likely contributed to our previous observation of denser ISGs (**Figure 4D**) (38). Exendin-4 stimulation led to the formation of more crystals, denser cores, and some ISGs with a smaller crystal-to-vesicle ratio than in the unstimulated condition (**Figure 4C-D**).

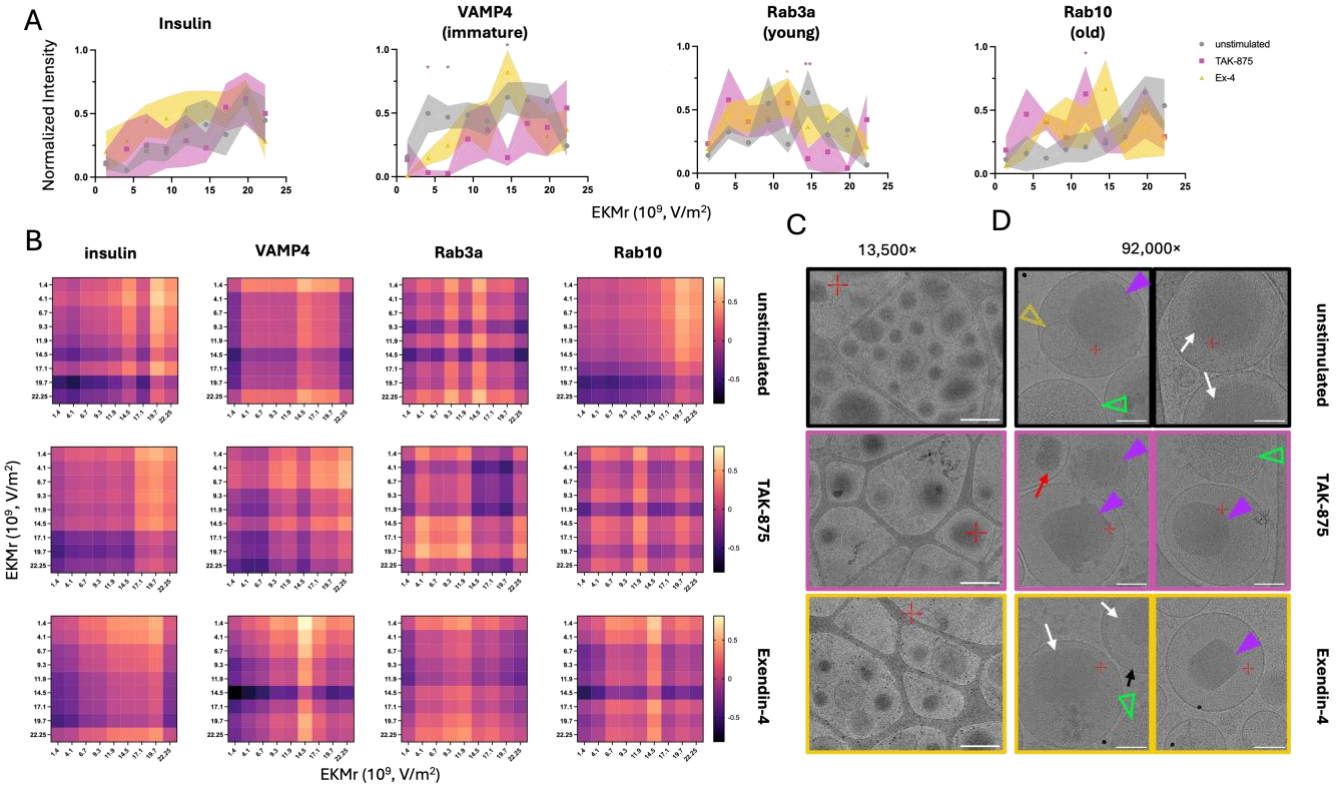

Figure 4. Comparison of ISG subpopulations between different stimulation conditions. **A.** EKMr distributions of ISGs isolated from unstimulated, TAK-875-stimulated (n=4 for 2 biologically independent experiments), and Ex-4-stimulated cells (n=4-7 for 2-3 biologically independent experiments). **B.** Heatmaps displaying the differences in average intensities between each pair of EKMr values within ISG subpopulation markers and unstimulated, TAK-875-stimulated, and Ex-4-stimulated conditions. **C-D.** Cryo-electron micrographs of ISGs inside unstimulated (top), Ex-4-stimulated (middle), and TAK-875-stimulated (bottom) mouse primary β-cells at **C.** 13,500x magnification, pixel size 2.06 nm, and **C.** 92,000x magnification, pixel size 0.15 nm. **D.** Symbols depict vesicles inside ISGs (yellow, double-lined arrowheads), crystalline cores (purple arrowheads), condensing cores (white arrows), immature ISGs (green, empty arrowheads), aggregates (red arrow), and fibrils (black arrow). Values are mean ± SEM (*$p\leq0.05$, **$p\leq0.01$ using ANOVA with Bonferroni post hoc multiple comparison correction. Comparisons made between stimulation and unstimulated condition, symbols color-coded according to condition). Scale bars: **C**: 500 nm; **D**: 100 nm.

DISCUSSION

Subpopulations of ISGs have varying sizes and contents, but the extent of these differences is unknown (5,6,16,38,39). In this work, our goal was to further develop separation methods and provide a more comprehensive analysis of the biophysical features of ISG subpopulations (35). In particular, we wanted to increase the interpretability of DC-iDEP separations by identifying the distribution of previously identified ISG subpopulations using Rab3a, Rab10, and VAMP4 antibodies to label young, old, and immature ISGs, as well as an insulin antibody to label all maturing ISGs (5,7). In this work, we found that these ISG subpopulations had characteristic distributions in unstimulated cells (**Figure 3A**).

Interpreting the Size of ISGs and EKMr distributions

The traditional view in the field is that immature ISGs tend to be larger and less dense than mature ISGs. EKMr values typically vary inversely with radius (**Equation 1**) (38,49,50). This correlates with immature ISGs displaying higher ratios of ISGs at lower EKMr values, whereas young and old ISGs displayed distribution peaks at higher EKMr values. Insulin-positive ISGs exhibited two peaks at high EKMr values, likely mostly consisting of smaller, more mature ISGs (**Figure 3A**). The differences in EKMr distributions are likely in part related to the expected differences in the size of ISGs between these populations due to the high impact of particle radius on EKMr.

Zeta potential and conductivity of ISGs and EKMr distributions

In addition to differences in size, variances in zeta potential and conductivity influence the EKMr value of a particle (**Equation 1**). It has been reported that young ISGs have lower zeta potentials and higher rigidities due to specific lipid compositions than older ISGs (5). These characteristics complement the distribution peaks at lower EKMr values of young ISGs than old ISGs in this work, with immature VAMP4 ISGs corresponding to low-EKMr values (**Figure 3A**). Changes in the pH of ISGs may also affect the EKMr distribution of ISGs. ISGs with lower pH, such as mature ISGs, may have a higher conductivity and therefore lower EKMr distributions (16,51). Further biophysical characterization of the ISG subpopulations is necessary to completely understand which protein and lipid species are most influential in subpopulation formation.

Heterogeneity within known subpopulations

In addition to the overall distribution trends, we observed multiple peaks or a broad distribution of ISGs at multiple EKMr values within each subpopulation we studied. This indicates that there is appreciable heterogeneity in the biophysical makeup of these ISG subpopulations. Thus, each of the known subpopulations contains a collection of physically distinct ISGs. Insulin-labeled ISGs exhibited two major peaks, overlapping with the higher-EKMr peaks seen in young and old subpopulations. We observed the most heterogeneity in immature and young ISGs, which may be due to activation of multiple maturation pathways giving rise to distinct subtypes over the lifetime of an ISG. VAMP4-positive ISGs had a broad distribution across the EKMr range tested, with a higher ratio of low-EKMr ISGs than other subpopulations (**Figure 3A, Figure S3C)**. The bimodal distribution of young ISGs indicates the presence of young ISGs with a crystalline core (1.45×10^{10} V/m^2) and young ISGs containing only condensed insulin (9.30×10^{9} V/m^2), as the subset of ISGs positive for Rab3a likely contains ISGs in various stages of maturity (5). The heterogeneity observed within immature, young, and old subpopulations may be due to the presence of other previously described ISG pools, such as synaptotagmin 7 (syt7) or synaptotagmin 9 (syt9) subpopulations (**Figure S8**) (6). These subpopulations have variations in their size, protein, and lipid compositions that would affect the EKMr distribution, while also likely existing in different maturation and age stages.

Impact of ISG maturation stimuli on ISG subpopulations

To better understand how different cellular pathways impact the generation of biophysically and functionally distinct ISG subtypes, we explored how lipid signaling and incretin signaling affect young, old, and immature ISGs. Two drugs that enhance maturation through distinct signaling pathways, TAK-875 and exendin-4, have previously been reported to affect ISG maturation, upregulating biophysically distinct ISG subpopulations (16,38,39). TAK-875 is associated with lipid signaling, and TAK-875 stimulation results in an increase in larger, denser ISGs that are often closer to the plasma membrane and distinct aggregate formations within the lumen (**Figure 4D)** (38,39). Ex-4 stimulation causes more condensed crystalline cores throughout the cell (**Figure 4C-D**) (38,39).

Stimulation by TAK-875 or Ex-4 did not result in significant changes in the distribution of insulin-labeled ISGs, although there was perhaps a higher ratio of low-EKMr to high-EKMr insulin-labeled ISGs in the Ex-4 condition (**Figure 4A**). The sum of the EKMr distributions of these subpopulations does not overlay with the distribution of insulin as cleanly as in the unstimulated condition (**Figure S5**), which suggests that there are different ratios of these subpopulations within the cell in response to TAK-875 and Ex-4. We saw a decrease in the subset of ISGs containing VAMP4 with low EKMr values in response to TAK-875 (**Figure 4A**), consistent with an increase in mature ISGs. Stimulation with TAK-875 also resulted in an increased proportion of low-EKMr young and old ISGs, but fewer immature ISGs compared to the unstimulated condition. This may indicate a rise in the radius of mature ISGs in response to TAK-875, consistent with previous studies. Stimulation with Ex-4 results in increased ISG maturation,

decreased ISG diameter, and decreased ISG pH (16,38,39). We observed a decrease in low-EKMr VAMP4 ISGs, as well as a significant increase in young ISGs at 1.19×10^{10} V/m^2, in response to Ex-4 (**Figure 4A**), indicating a decrease in immature ISGs and likely an increase in smaller, mature ISGs containing crystalline insulin. There were decreases in the amount of old ISGs at 1.97×10^{10} V/m^2 in response to both Ex-4 and TAK-875. These decreases, while slight, may indicate remodeling of not only immature and newly formed ISGs, but also old ISGs. Although some changes in old ISGs may be due to recent ISG secretion, β-cells preferentially secrete young ISGs, potentially due to caging of old ISGs (16,21). For the distribution of old ISGs to change in response to TAK-875 and Ex-4, there must be some transformation or degradation of old ISGs.

TAK-875 stimulation likely causes more significant changes than Ex-4 stimulation due to potential lipid remodeling of the ISG membrane, resulting in changes in size and surface charges of ISGs (38). As the field learns more about inter-organelle contacts and communication, we will be able to piece together how these physical changes occur and what proteins are involved in regulating ISG maturation. Especially considering that different cellular signals impact ISG biophysical characteristics, it is clear that there are multiple pathways for maturation and a diverse range of ISGs that the cell can generate.

Future exploration of the effect of diseased states may improve our understanding of the functional implications of these changes, as certain subpopulations are known to be associated with either type 1 or type 2 diabetes (6). Identifying any overlap between the subpopulations described here and disease-related pools may enable a better understanding of these conditions and the development of future treatments. This method may also prove useful in studying heterogeneity in other organelles or cells (52-58).

Limitations of the study

In order to separate ISG subpopulations by DC-iDEP, ISGs must be removed from the cellular environment, which prevents correlation of EKMr values of an ISG with its native surroundings. Additionally, it can be challenging to isolate all ISGs for analysis. Immature ISGs lack the dense core that mature ISGs have and are found in different fractions than mature ISGs when isolated via traditional methods like density gradient columns (7). To address this challenge, future development of the separation channel to allow for the removal of separated subpopulations would enable the identification of more specific subpopulation markers. Labelling and imaging these specific markers *in cellulo* would assist in the interpretation of the identities of the separated subpopulations. Additionally, modifying the channel to increase the resolution of mid-to-high EKMr values may improve the separation of ISG subpopulations. Because DC-iDEP provides higher sensitivity separations, further development as a preparative tool has powerful potential to methodically explore biophysical heterogeneity of ISGs, viruses, or other biologically complex particles. INS-1E cells were used as a model of β-cells in this study for their ease of use and scalability, but the use of primary mouse or human β-cells may provide more insight into the heterogeneity of ISGs during disease progression. Primary β-cells appear to contain more crystalline insulin in their ISGs (**Figure S9**), which would likely affect EKMr distribution. They also contain other components that might affect the EKMr distribution, such as fibrils, aggregates, and vesicles (**Figure 4C-D**).

The markers we used likely label several types of ISG within the major subpopulations studied. Additionally, the antibodies themselves may alter the EKMr of the ISGs they label. Each of these factors provides challenges in data interpretation, which may be made simpler by future technological advances. Despite these complications, these results provide new insights into the heterogeneity of ISGs and provide a basis for further use of DC-iDEP for exploring biological particles.

RESOURCE AVAILABILITY

Lead Contact

Kate L. White, katewhit@usc.edu

AUTHOR CONTRIBUTIONS

Conceptualization, A.A. and K.L.W.; methodology, A.A., T.K., M.A.H., K.L.W.; investigation, A.A., T.K., A.D.; writing—initial draft, A.A. and K.L.W., writing—review & editing, A.A., K.L.W., T.K., A.D., M.A.H.; funding acquisition, K.L.W.; resources, K.L.W and M.A.H.; supervision, K.L.W. and M.A.H.

ACKNOWLEDGMENTS

This material is based upon work supported by the National Science Foundation Graduate Research Fellowship Program under Grant No. DGE-1842487. Any opinions, findings, and conclusions or recommendations expressed in this material are those of the author(s) and do not necessarily reflect the views of the National Science Foundation. Funding from the National Institute of General Medical Sciences of the National Institutes of Health, under award number R35GM154893, and the USC Bridge Institute at USC provided financial support for this work. Thank you to Kevin Chang and Janielle Cuala for providing mouse islets for CryoEM experiments and Yekaterina Kadyshevskaya for illustration assistance. Thank you to Alex Ramirez for assisting in setting up the DEP device at USC. Human pancreatic islets were provided by the NIDDK-funded Integrated Islet Distribution Program (IIDP) (RRID:SCR_014387) at City of Hope, NIH Grant # U24DK098085. Images presented in this article were acquired at the Core Center of Excellence in Nano Imaging at the University of Southern California.

DECLARATION OF INTERESTS

MAH declares a conflict of interest with CBio where he serves as the CSO, and with Hayes Diagnostics, Inc, where he serves as COB, CEO & CSO. All other authors have no conflict of interest to declare. The other authors declare that they have no competing interests.

REFERENCES

1. Petersen, M. C., and G. I. Shulman. 2018. Mechanisms of Insulin Action and Insulin Resistance. *Physiol Rev*. 98(4):2133-2223, doi: 10.1152/physrev.00063.2017.
2. Hou, J. C., L. Min, and J. E. Pessin. 2009. Insulin granule biogenesis, trafficking and exocytosis. *Vitam Horm*. 80:473-506, doi: 10.1016/S0083-6729(08)00616-X, https://www.ncbi.nlm.nih.gov/pubmed/19251047.
3. Arvan, P., and D. Castle. 1998. Sorting and storage during secretory granule biogenesis: looking backward and looking forward. *Biochem J*. 332 (Pt 3)(Pt 3):593-610, doi: 10.1042/bj3320593.
4. Dodson, G., and D. Steiner. 1998. The role of assembly in insulin's biosynthesis. *Curr Opin Struct Biol*. 8(2):189-194, doi: 10.1016/s0959-440x(98)80037-7.
5. Neukam, M., P. Sala, A. D. Brunner, K. Ganss, A. Palladini, M. Grzybek, O. Topcheva, J. Vasiljevic, J. Broichhagen, K. Johnsson, T. Kurth, M. Mann, U. Coskun, and M. Solimena. 2024. Purification of time-resolved insulin granules reveals proteomic and lipidomic changes during granule aging. *Cell Rep*. 43(3):113836, doi: 10.1016/j.celrep.2024.113836, https://www.ncbi.nlm.nih.gov/pubmed/38421874.
6. Kreutzberger, A. J. B., V. Kiessling, C. A. Doyle, N. Schenk, C. M. Upchurch, M. Elmer-Dixon, A. E. Ward, J. Preobraschenski, S. S. Hussein, W. Tomaka, P. Seelheim, I. Kattan, M. Harris, B. Liang, A. K. Kenworthy, B. N. Desai, N. Leitinger, A. Anantharam, J. D. Castle, and L. K. Tamm. 2020. Distinct insulin granule subpopulations implicated in the secretory pathology of diabetes types 1 and 2. *Elife*. 9, doi: 10.7554/eLife.62506, https://www.ncbi.nlm.nih.gov/pubmed/33164744.
7. Norris, N., B. Yau, and M. A. Kebede. 2021. Isolation and Proteomics of the Insulin Secretory Granule. *Metabolites*. 11(5), doi: 10.3390/metabo11050288, https://www.ncbi.nlm.nih.gov/pubmed/33946444.
8. Vasiljevic, J., J. M. Torkko, K. P. Knoch, and M. Solimena. 2020. The making of insulin in health and disease. *Diabetologia*. 63(10):1981-1989, doi: 10.1007/s00125-020-05192-7, https://www.ncbi.nlm.nih.gov/pubmed/32894308.
9. DJ, M., and B. EJ. 2021. Chapter 3: Global Picture. In IDF Diabetes Atlas. International Diabetes Federation.
10. Olofsson, C. S., S. O. Göpel, S. Barg, J. Galvanovskis, X. Ma, A. Salehi, P. Rorsman, and L. Eliasson. 2002. Fast insulin secretion reflects exocytosis of docked granules in mouse pancreatic B-cells. *Pflügers Archiv*. 444(1):43-51, doi: 10.1007/s00424-002-0781-5, https://doi.org/10.1007/s00424-002-0781-5.
11. Olofsson, C. S., A. Salehi, C. Holm, and P. Rorsman. 2004. Palmitate increases L-type Ca2+ currents and the size of the readily releasable granule pool in mouse pancreatic β-cells. *The Journal of Physiology*. 557(3):935-948, doi: https://doi.org/10.1113/jphysiol.2004.066258, https://physoc.onlinelibrary.wiley.com/doi/abs/10.1113/jphysiol.2004.066258.
12. Pottekat, A., S. Becker, Kathryn R. Spencer, John R. Yates, G. Manning, P. Itkin-Ansari, and William E. Balch. 2013. Insulin Biosynthetic Interaction Network Component, TMEM24, Facilitates Insulin Reserve Pool Release. *Cell Reports*. 4(5):921-930, doi: 10.1016/j.celrep.2013.07.050.
13. Daniel, S., M. Noda, S. G. Straub, and G. W. Sharp. 1999. Identification of the docked granule pool responsible for the first phase of glucose-stimulated insulin secretion. *Diabetes*. 48(9):1686-1690, doi: 10.2337/diabetes.48.9.1686, https://doi.org/10.2337/diabetes.48.9.1686.

14. Hao, M., X. Li, M. A. Rizzo, J. V. Rocheleau, B. M. Dawant, and D. W. Piston. 2005. Regulation of two insulin granule populations within the reserve pool by distinct calcium sources. *Journal of Cell Science*. 118(24):5873-5884, doi: 10.1242/jcs.02684, https://doi.org/10.1242/jcs.02684.
15. Omar-Hmeadi, M., and O. Idevall-Hagren. 2021. Insulin granule biogenesis and exocytosis. *Cell Mol Life Sci*. 78(5):1957-1970, doi: 10.1007/s00018-020-03688-4, https://www.ncbi.nlm.nih.gov/pubmed/33146746.
16. Lin, W., K. Tseng, S. E. Fraser, J. Junge, and K. L. White. 2024. Decoding Insulin Secretory Granule Maturation Using Genetically Encoded pH Sensors. *ACS Sens*. 9(11):6032-6039, doi: 10.1021/acssensors.4c01885, https://www.ncbi.nlm.nih.gov/pubmed/39504473.
17. Li, M., F. Feng, H. Feng, P. Hu, Y. Xue, T. Xu, and E. Song. 2022. VAMP4 regulates insulin levels by targeting secretory granules to lysosomes. *Journal of Cell Biology*. 221(10), doi: 10.1083/jcb.202110164, https://doi.org/10.1083/jcb.202110164.
18. Halban, P. A. 1982. Differential Rates of Release of Newly Synthesized and of Stored Insulin from Pancreatic Islets. *Endocrinology*. 110:1183-1188, Suppl 4, doi: 10.1210/endo-110-4-1183.
19. Gold, G., M. L. Gishizky, and G. M. Grodsky. 1982. Evidence That Glucose "Marks" β Cells Resulting in Preferential Release of Newly Synthesized Insulin. *Science*. 218:56-58, doi: 10.1126/science.61815.
20. Schatz, H., C. Nierle, and E. F. Pfeiffer. 1975. (Pro-)Insulin Biosynthesis and Release of Newly Synthesized (Pro-)Insulin from Isolated Islets of Rat Pancreas in the Presence of Amino Acids and Sulphonylureas. *European Journal of Clinical Investigation*. 5(6):477-485, doi: https://doi.org/10.1111/j.1365-2362.1975.tb02312.x, https://onlinelibrary.wiley.com/doi/abs/10.1111/j.1365-2362.1975.tb02312.x.
21. Yau, B., L. Hays, C. Liang, D. R. Laybutt, H. E. Thomas, J. E. Gunton, L. Williams, W. J. Hawthorne, P. Thorn, C. J. Rhodes, and M. A. Kebede. 2020. A fluorescent timer reporter enables sorting of insulin secretory granules by age. *J Biol Chem*. 295(27):8901-8911, doi: 10.1074/jbc.RA120.012432, https://www.ncbi.nlm.nih.gov/pubmed/32341128.
22. Arous, C., and P. A. Halban. 2015. The skeleton in the closet: actin cytoskeletal remodeling in β-cell function. *American Journal of Physiology-Endocrinology and Metabolism*. 309(7):E611-E620, doi: 10.1152/ajpendo.00268.2015, https://journals.physiology.org/doi/abs/10.1152/ajpendo.00268.2015.
23. Tooze, S. A., T. Flatmark, J. Tooze, and W. B. Huttner. 1991. Characterization of the immature secretory granule, an intermediate in granule biogenesis. *Journal of Cell Biology*. 115(6):1491-1503, doi: 10.1083/jcb.115.6.1491, https://doi.org/10.1083/jcb.115.6.1491.
24. Li, M., W. Du, M. Zhou, L. Zheng, E. Song, and J. Hou. 2018. Proteomic analysis of insulin secretory granules in INS-1 cells by protein correlation profiling. *Biophys Rep*. 4(6):329-338, doi: 10.1007/s41048-018-0061-3, https://www.ncbi.nlm.nih.gov/pubmed/30596141.
25. MacDonald, M. J., L. Ade, J. M. Ntambi, I. U. Ansari, and S. W. Stoker. 2015. Characterization of phospholipids in insulin secretory granules and mitochondria in pancreatic beta cells and their changes with glucose stimulation. *J Biol Chem*. 290(17):11075-11092, doi: 10.1074/jbc.M114.628420, https://www.ncbi.nlm.nih.gov/pubmed/25762724.
26. Hickey, A. J. R., J. W. I. Bradley, G. L. Skea, M. J. Middleditch, C. M. Buchanan, A. R. J. Phillips, and G. J. S. Cooper. 2009. Proteins Associated with Immunopurified Granules from a Model Pancreatic Islet β-Cell System: Proteomic Snapshot of an Endocrine Secretory Granule. *Journal of Proteome Research*. 8(1):178-186, doi: 10.1021/pr800675k, https://doi.org/10.1021/pr800675k.
27. Guest, P. C. 2017. Multiplex Sequential Immunoprecipitation of Insulin Secretory Granule Proteins from Radiolabeled Pancreatic Islets. *Methods Mol Biol*. 1546:177-185, doi: 10.1007/978-1-4939-6730-8_14.
28. Albrethsen, J., J. P. Goetze, and A. H. Johnsen. 2015. Mining the Granule Proteome: A Potential Source of Endocrine Biomarkers. *Biomarkers in Medicine*. 9(3):259-265, doi: 10.2217/bmm.14.107, https://doi.org/10.2217/bmm.14.107.
29. Brunner, Y., Y. Coute, M. Iezzi, M. Foti, M. Fukuda, D. F. Hochstrasser, C. B. Wollheim, and J. C. Sanchez. 2007. Proteomics analysis of insulin secretory granules. *Mol Cell Proteomics*. 6(6):1007-1017, doi: 10.1074/mcp.M600443-MCP200, https://www.ncbi.nlm.nih.gov/pubmed/17317658.
30. Schvartz, D., Y. Brunner, Y. Coute, M. Foti, C. B. Wollheim, and J. C. Sanchez. 2012. Improved characterization of the insulin secretory granule proteomes. *J Proteomics*. 75(15):4620-4631, doi: 10.1016/j.jprot.2012.04.023, https://www.ncbi.nlm.nih.gov/pubmed/22569486.
31. Zhu, F., B. L. Nannenga, and M. A. Hayes. 2019. Electrophoretic exclusion microscale sample preparation for cryo-EM structural determination of proteins. *Biomicrofluidics*. 13(5):054112, doi: 10.1063/1.5124311.

32. Liu, Y., A. Jiang, E. Kim, C. Ro, T. Adams, L. A. Flanagan, T. J. Taylor, and M. A. Hayes. 2019. Identification of neural stem and progenitor cell subpopulations using DC insulator-based dielectrophoresis. *Analyst*. 144(13):4066-4072, doi: 10.1039/c9an00456d, https://www.ncbi.nlm.nih.gov/pubmed/31165125.
33. Liu, Y., and M. A. Hayes. 2020. Differential Biophysical Behaviors of Closely Related Strains of Salmonella. *Frontiers in Microbiology*. Volume 11 - 2020, doi: 10.3389/fmicb.2020.00302, https://www.frontiersin.org/journals/microbiology/articles/10.3389/fmicb.2020.00302 (Original Research).
34. Ramirez, A. J., A. K. M. F. K. Rasel, S. L. Seyler, and M. A. Hayes. 2025. Gradient Insulator-Based Dielectrophoresis of Gold Nanoparticles. *ELECTROPHORESIS*. 46(11-12):768-776, doi: https://doi.org/10.1002/elps.8119, https://analyticalsciencejournals.onlinelibrary.wiley.com/doi/abs/10.1002/elps.8119.
35. Barekatain, M., Y. Liu, A. Archambeau, V. Cherezov, S. Fraser, K. L. White, and M. A. Hayes. 2024. Insulator-based dielectrophoresis-assisted separation of insulin secretory vesicles. *eLife*. 13:e74989, doi: 10.7554/eLife.74989, https://doi.org/10.7554/eLife.74989.
36. Crowther, C. V., V. Sanderlin, M. A. Hayes, and G. H. Gile. 2019. Effects of surface treatments on trapping with DC insulator-based dielectrophoresis. *Analyst*. 144(24):7478-7488, doi: 10.1039/c9an01186b, https://www.ncbi.nlm.nih.gov/pubmed/31720589.
37. Nauck, M. A., and J. J. Meier. 2018. Incretin hormones: Their role in health and disease. *Diabetes Obes Metab*. 20 Suppl 1:5-21, doi: 10.1111/dom.13129.
38. Deshmukh, A., K. Chang, J. Cuala, M. J. Hernandez Campos, S. Mahmood, R. Verma, S. Georgia, V. Loconte, and K. L. White. 2025. Secretory stimuli distinctly regulate insulin secretory granule maturation through structural remodeling. *Structure*. doi: 10.1016/j.str.2025.07.022, https://doi.org/10.1016/j.str.2025.07.022.
39. Chang, K. S., K. L. White, A. Deshmukh, R. Verma, and V. Loconte. 2025. Classifying Biophysical Subpopulations of Insulin Secretory Granules using Quantitative Whole Cell Structure Analysis. *bioRxiv*.2025.2009.2009.675239, doi: 10.1101/2025.09.09.675239, https://www.biorxiv.org/content/biorxiv/early/2025/09/15/2025.09.09.675239.full.pdf.
40. Dong, T. X., S. Othy, A. Jairaman, J. Skupsky, A. Zavala, I. Parker, J. L. Dynes, and M. D. Cahalan. 2017. T-cell calcium dynamics visualized in a ratiometric tdTomato-GCaMP6f transgenic reporter mouse. *Elife*. 6, doi: 10.7554/eLife.32417.
41. Staton, S. J. R., K. P. Chen, T. J. Taylor, J. R. Pacheco, and M. A. Hayes. 2010. Characterization of particle capture in a sawtooth patterned insulating electrokinetic microfluidic device. *ELECTROPHORESIS*. 31(22):3634-3641, doi: https://doi.org/10.1002/elps.201000438, https://analyticalsciencejournals.onlinelibrary.wiley.com/doi/abs/10.1002/elps.201000438.
42. Schindelin, J., I. Arganda-Carreras, E. Frise, V. Kaynig, M. Longair, T. Pietzsch, S. Preibisch, C. Rueden, S. Saalfeld, B. Schmid, J.-Y. Tinevez, D. J. White, V. Hartenstein, K. Eliceiri, P. Tomancak, and A. Cardona. 2012. Fiji: an open-source platform for biological-image analysis. *Nature Methods*. 9(7):676-682, doi: 10.1038/nmeth.2019, https://doi.org/10.1038/nmeth.2019.
43. Zhang, X., S. D. Carter, J. Singla, K. L. White, P. C. Butler, R. C. Stevens, and G. J. Jensen. 2020. Visualizing insulin vesicle neighborhoods in beta cells by cryo-electron tomography. *Sci Adv*. 6(50), doi: 10.1126/sciadv.abc8258, https://www.ncbi.nlm.nih.gov/pubmed/33298442.
44. Ivanova, A., Y. Kalaidzidis, R. Dirkx, M. Sarov, M. Gerlach, B. Schroth-Diez, A. Müller, Y. Liu, C. Andree, B. Mulligan, C. Münster, T. Kurth, M. Bickle, S. Speier, K. Anastassiadis, and M. Solimena. 2013. Age-Dependent Labeling and Imaging of Insulin Secretory Granules. *Diabetes*. 62(11):3687-3696, doi: 10.2337/db12-1819, https://doi.org/10.2337/db12-1819.
45. Izumi, T. 2023. Multiple pathways and independent functional pools in insulin granule exocytosis. *Genes to Cells*. 28(7):471-481, doi: https://doi.org/10.1111/gtc.13029, https://onlinelibrary.wiley.com/doi/abs/10.1111/gtc.13029.
46. Varadi, A., T. Tsuboi, and G. A. Rutter. 2005. Myosin Va Transports Dense Core Secretory Vesicles in Pancreatic MIN6 β-Cells. *Molecular Biology of the Cell*. 16(6):2670-2680, doi: 10.1091/mbc.e04-11-1001, https://www.molbiolcell.org/doi/abs/10.1091/mbc.e04-11-1001.
47. Wang, X., G. Arpino, A. Mohseni, C. K. E. Bleck, and L.-G. Wu. 2025. Dense-core vesicles contain exosomes in secretory cells. *Biophysical Journal*. 124(11):1747-1752, doi: 10.1016/j.bpj.2025.01.003, https://doi.org/10.1016/j.bpj.2025.01.003.

48. Greider , M. H., S. L. Howell , and P. E. Lacy 1969. ISOLATION AND PROPERTIES OF SECRETORY GRANULES FROM RAT ISLETS OF LANGERHANS : II. Ultrastructure of the Beta Granule. *Journal of Cell Biology*. 41(1):162-166, doi: 10.1083/jcb.41.1.162, https://doi.org/10.1083/jcb.41.1.162.
49. Orci, L., M. Ravazzola, M. Amherdt, A. Perrelet, S. K. Powell, D. L. Quinn, and H.-P. H. Moore. 1987. The trans-most cisternae of the Golgi complex: A compartment for sorting of secretory and plasma membrane proteins. *Cell*. 51(6):1039-1051, doi: 10.1016/0092-8674(87)90590-3, https://doi.org/10.1016/0092-8674(87)90590-3.
50. Arvan, P., and P. A. Halban. 2004. Sorting ourselves out: seeking consensus on trafficking in the beta-cell. *Traffic*. 5(1):53-61, doi: 10.1111/j.1600-0854.2004.00152.x.
51. Orci, L., M. Ravazzola, M. Amherdt, O. Madsen, A. Perrelet, J. D. Vassalli, and R. G. Anderson. 1986. Conversion of proinsulin to insulin occurs coordinately with acidification of maturing secretory vesicles. *Journal of Cell Biology*. 103(6):2273-2281, doi: 10.1083/jcb.103.6.2273, https://doi.org/10.1083/jcb.103.6.2273.
52. Koch, M., L. Varela, J. G. Kim, J. D. Kim, F. Hernández-Nuño, S. E. Simonds, C. M. Castorena, C. R. Vianna, J. K. Elmquist, Y. M. Morozov, P. Rakic, I. Bechmann, M. A. Cowley, K. Szigeti-Buck, M. O. Dietrich, X.-B. Gao, S. Diano, and T. L. Horvath. 2015. Hypothalamic POMC neurons promote cannabinoid-induced feeding. *Nature*. 519(7541):45-50, doi: 10.1038/nature14260, https://doi.org/10.1038/nature14260.
53. Willms, E., C. Cabañas, I. Mäger, M. J. A. Wood, and P. Vader. 2018. Extracellular Vesicle Heterogeneity: Subpopulations, Isolation Techniques, and Diverse Functions in Cancer Progression. *Frontiers in Immunology*. Volume 9 - 2018, doi: 10.3389/fimmu.2018.00738, https://www.frontiersin.org/journals/immunology/articles/10.3389/fimmu.2018.00738 (Review).
54. Combe, M., K. S. Isaac, J. R. Plews, and S. Sokolenko. 2025. Quantifying extracellular vesicle heterogeneity: the effect of process conditions on protein cargo for skin therapy. *Stem Cell Res Ther*. 16(1):224, doi: 10.1186/s13287-025-04279-5.
55. Shaabani, N., S. R. Meira, M. Marcet-Palacios, and M. Kulka. 2023. Multiparametric Biosensors for Characterizing Extracellular Vesicle Subpopulations. *ACS Pharmacol Transl Sci*. 6(3):387-398, doi: 10.1021/acsptsci.2c00207, https://www.ncbi.nlm.nih.gov/pubmed/36926451.
56. Kravets, V., J. M. Dwulet, W. E. Schleicher, D. J. Hodson, A. M. Davis, L. Pyle, R. A. Piscopio, M. Sticco-Ivins, and R. K. P. Benninger. 2022. Functional architecture of pancreatic islets identifies a population of first responder cells that drive the first-phase calcium response. *PLoS Biol*. 20(9):e3001761, doi: 10.1371/journal.pbio.3001761, https://www.ncbi.nlm.nih.gov/pubmed/36099294.
57. Sterk, M., J. Dolensek, M. Skelin Klemen, L. Krizancic Bombek, E. Paradiz Leitgeb, J. Kercmar, M. Perc, M. Slak Rupnik, A. Stozer, and M. Gosak. 2023. Functional characteristics of hub and wave-initiator cells in beta cell networks. *Biophys J*. 122(5):784-801, doi: 10.1016/j.bpj.2023.01.039, https://www.ncbi.nlm.nih.gov/pubmed/36738106.
58. Duh, M., M. Šterk, L. Križančić Bombek, P. E. MacDonald, A. Stožer, and M. Gosak. 2025. Spatially bound functional heterogeneity drives modular organization in β-cell networks. *Biophysical Journal*. 124(18):3008-3022, doi: 10.1016/j.bpj.2025.07.043, https://doi.org/10.1016/j.bpj.2025.07.043.

SUPPLEMENTAL INFORMATION

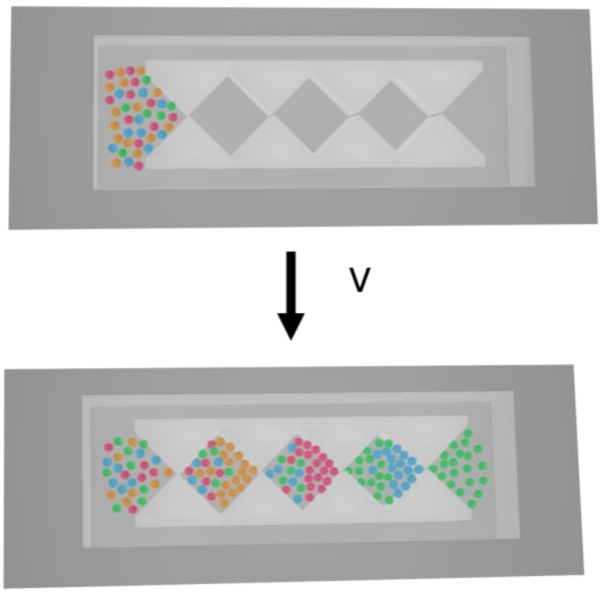

Figure S 1. A truncated model of the separation device showing heterogeneous particles before (top) and after applying a voltage to separate particles (bottom).

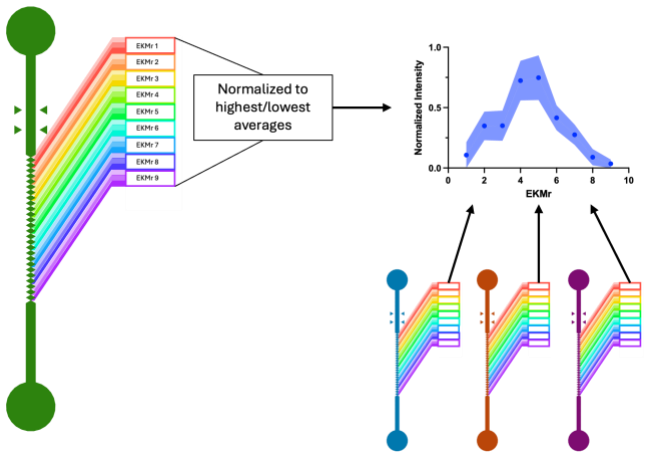

Figure S2. Schematic for normalizing DC-iDEP intensity data.

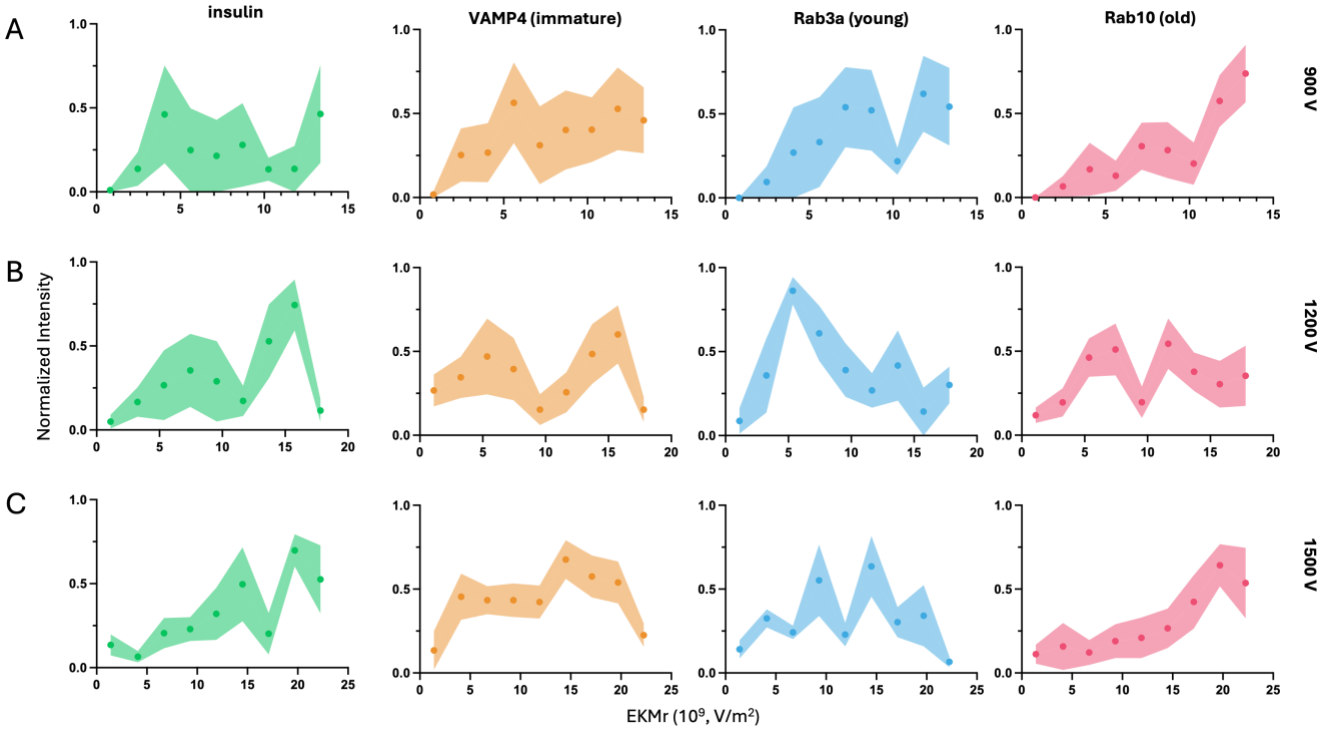

Figure S3. The EKMr distribution of different ISG subpopulations at **A.** 900 V, **B.** 1200 V, and **C.** 1500 V. Values are mean ± SEM.

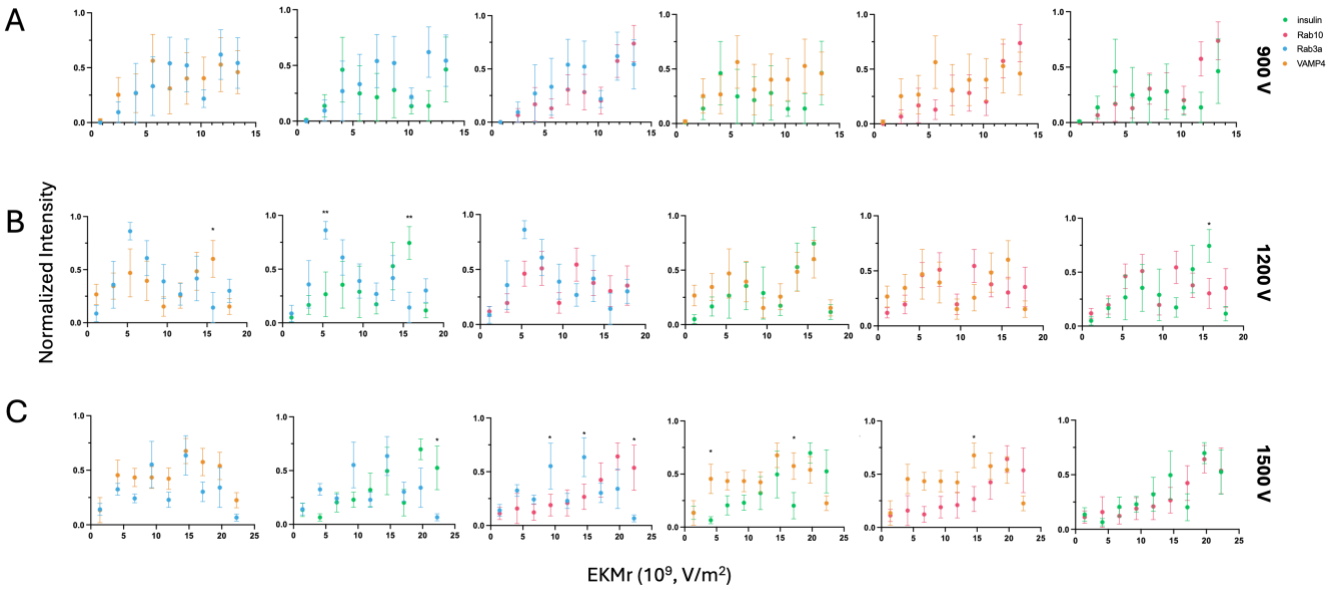

Figure S4. Comparisons of ISG subpopulation distributions at **A.** 900 V, **B.** 1200 V, and **C.** 1500 V. Values are mean ± SEM (*p≤0.05, **p≤0.01 using ANOVA with Bonferroni post hoc multiple comparison correction).

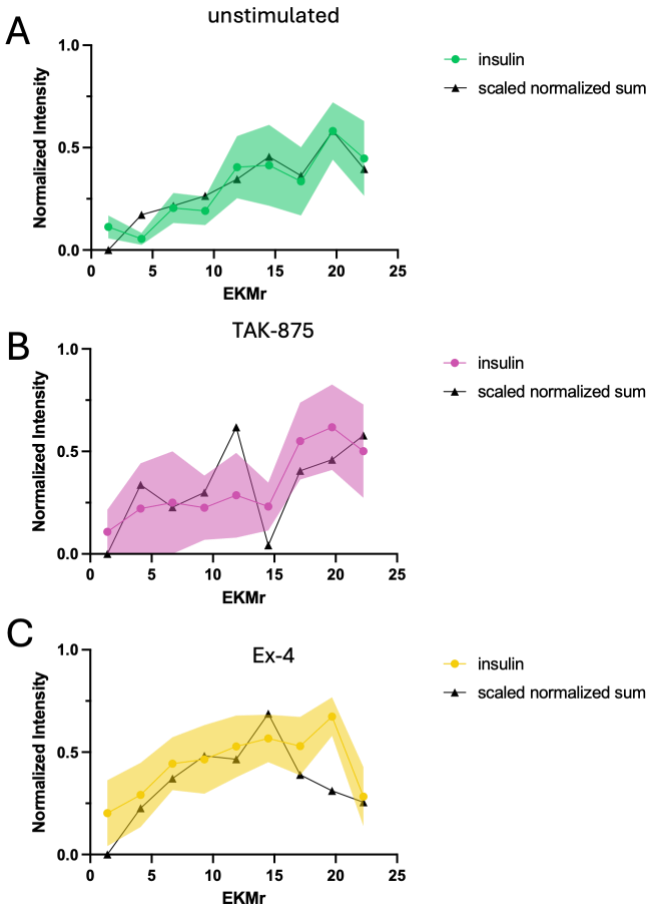

Figure S5. Comparisons of the EKMr distribution of insulin with the normalized sum of Rab3a, VAMP4, and Rab10 in the **A.** unstimulated, **B.** TAK-875-stimulated, and **C.** Ex-4-stimulated conditions. Values are mean ± SEM, and lines connect points for comprehensibility.

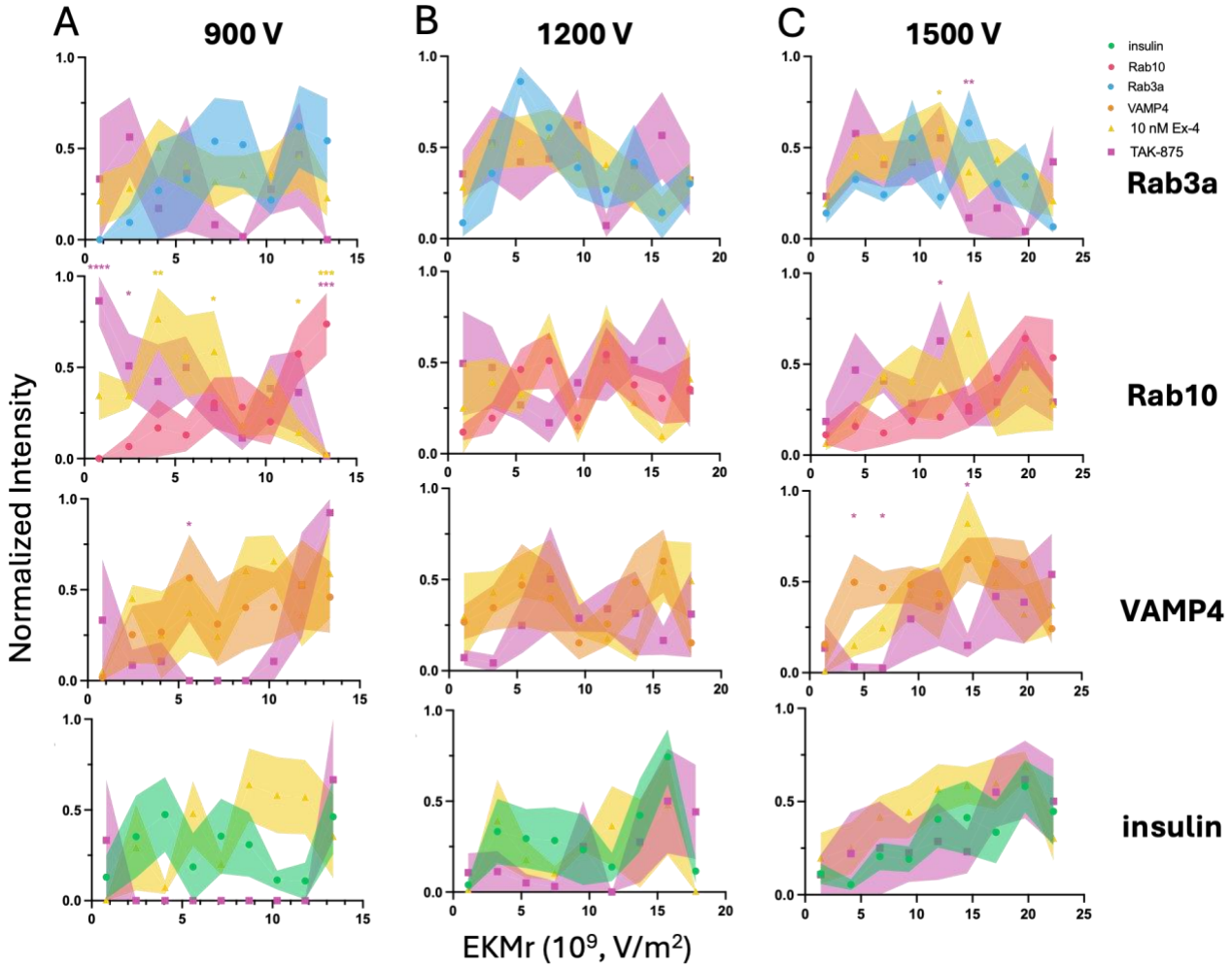

Figure S6. Changes in the EKMr distribution of each ISG subpopulation in response to TAK-875 and Ex-4 at **A.** 900 V, **B.** 1200 V, and **C.** 1500 V. Values are mean ± SEM (*p≤0.05, **p≤0.01, ***p≤0.001 using ANOVA with Bonferroni post hoc multiple comparison correction. Comparisons made between stimulation and unstimulated conditions, symbols color-coded according to condition).

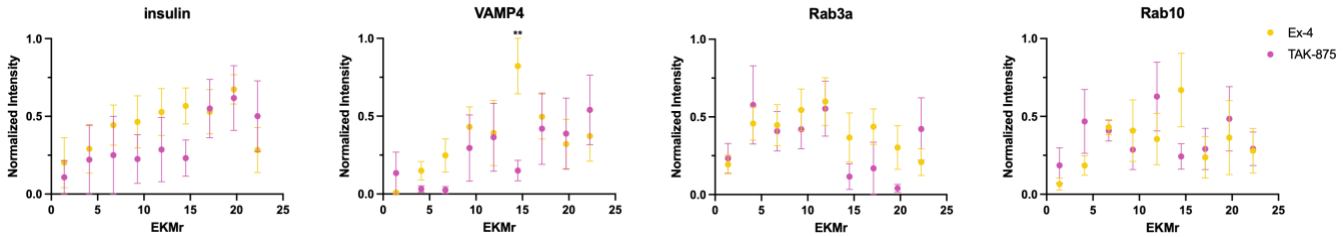

Figure S7. Differences in EKMr distributions between ISGs isolated from TAK-875 and Ex-4-stimulated cells. Values are mean ± SEM.

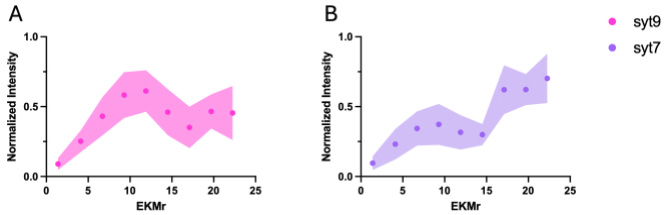

Figure S8. EKMr distributions of **A.** synaptotagmin 9 (syt9) and **B.** synaptotagmin 7 (syt7) at 1500 V. Values are mean ± SEM.

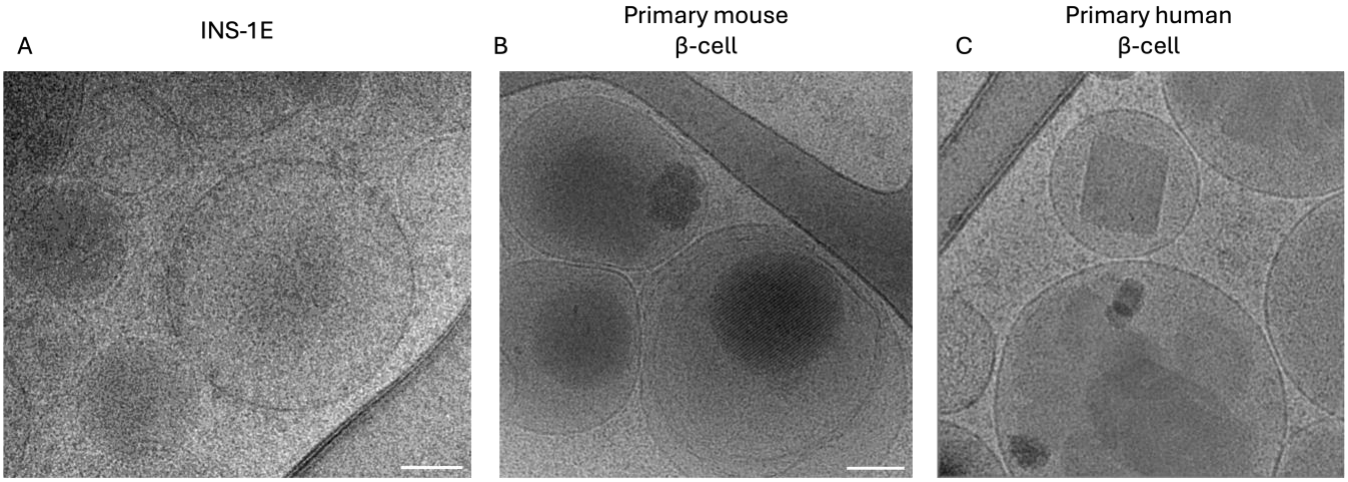

Figure S9. CryoEM images of ISGs inside INS-1E, primary mouse β-cells, and primary human β-cells. Magnification: **A-B.** 26,000x, **C.** 92,000x. Pixel size: **A-B.** 0.341 nm, **C.** 0.15 nm. A Gaussian blur of 1.0 nm was applied for clarity.